Article:
Al-Jazzar, SO, Aldalahmeh, SA, McLernon, D orcid.org/0000-0002-5163-1975 et al. (1 more author) (2020) Intruder Localization and Tracking Using Two Pyroelectric Infrared Sensors. IEEE Sensors Journal, 20 (11). pp. 6075-6082. ISSN 1530-437X

https://doi.org/10.1109/jsen.2020.2974633

Intruder Localization and Tracking Using Two Pyroelectric Infrared Sensors

Saleh O. Al-Jazzar, Sami A. Aldalahmeh, *Member, IEEE,* Des McLernon, *Member, IEEE,* and Syed Ali Raza Zaidi, *Member, IEEE*

***Abstract*—In this paper, we introduce a method to estimate the range of an intruder and track its trajectory by utilizing the received signal strength of the heat flux for pyroelectric infrared (PIR) sensors. To this end, we first develop a mathematical model of the received heat flux signal strength and the corresponding PIR signal for a moving intruder. The algorithm uses only two PIR sensors and the geometry of the field of views (FOVs) to perform the estimation and tracking process without any knowledge of the intruder's parameters. The tracking algorithm shows remarkable performance in estimating the intruder's parameters. The intruder heat flux was accurately estimated even at large separation distances as was the intruder path angle. Finally, the intruder's location was also very accurately estimated with sub-meter error for large separation distances.**

***Index Terms*—Pyroelectric infrared sensor, localization, tracking, received signal strength.**

I. Introduction

Localization and tracking of intruders are vital aspects of any surveillance system. A range of different sensing technologies including, magnetic, acoustic, seismic and thermal sensors [1] have been employed for provisioning such a surveillance functionality. Infrared sensors, in particular, are used in many applications [2], especially localization [3]. However pyroelectric infrared (PIR) sensors [4] render themselves as a promising choice due to their low power requirement, low cost and small form factor.

Recently, PIR sensors have been used in low-range indoor applications, such as hand gesture recognition [5], [6]. Also, PIR sensors have been used for assisted living applications with a combination of other sensors (see [7] and references therein). PIR sensors have been extensively employed in the context of human tracking and classification. Interested readers are referred to [8]–[12] for details. The PIR sensors are also instrumented in several outdoor applications such as critical area surveillance [13] and intrusion classification [14]. More recently, a combination of PIR and seismic sensors has been used for target classification in [15]. Similarly, PIR and ultrasonic sensors were used for flash flood detection in [16]. The previous sensor combination was also used for traffic monitoring systems in [17], in which both sensors' data are fused to detect and estimate vehicle velocity.

Saleh O. Al-Jazzar and Sami A. Aldalahmeh are with the Faculty of Engineering and Technology in the Al-Zaytoonah University of Jordan, Amman Jordan (email: saleh.g@zuj.edu.jo, s.aldalahmeh@zuj.edu.jo).

Des McLernon and Syed Ali Raza Zaidi are with the School of Electronic and Electrical Engineering in Leeds University, Leeds, UK (email: d.c.mclernon@leeds.ac.uk, s.a.zaidi@leeds.ac.uk).

This work was supported by Al-Zaytoonah University of Jordan through the grant 13/28/2017-2018.

Obviously, the PIR sensor signal provides a valuable source of information that can be used for detection, localization and classification of pedestrians [10] and vehicles [17]. Several processing methods have been suggested in the literature to extract such information. In [18], energy detection with an adaptive noise threshold was proposed. Simple high-pass filtering was also used to improve the signal-to-noise ratio (SNR). A combination of the Haar transform and support-vector-machine was used in [19] to detect intrusion in the presence of clutter. In [20], the authors proposed using probabilistic nonnegative matrix factorization (PNMF) as a learning mechanism to detect and classify human walking movement. The PIR sensors were assembled in arrays fitted in *towers* deployed on four walls of a room. PIR sensors were used for the tracking of direction and distance of motion in [21] via feature extraction methods. The sensor nodes were mounted on a hallway and reported back wirelessly to the base station. A set of two orthogonal PIR sensor pairs was used in [22] to detect the direction of movement, where the array was mounted in the ceiling. In [23], the authors suggested an enhanced detection range method via the windowed periodgram method, with a single PIR sensor.

In this paper, we propose an array of only two PIR sensors for intruder localization and tracking using the PIR sensors' signal strength together with the geometrical setting of the Fresnel lens field of views (FOVs) angles. This method does not assume the knowledge of any physical aspect of the intruder. Nor does it require a specific inter-sensor separation. Hence, the proposed method is suitable for various outdoor applications

The rest of the paper is organized as follows: Section II presents the modeling of the intruder signature. Section III presents the PIR signal processing chain. The proposed localization algorithm is given in Section IV. Simulation results are introduced in Section V. Finally, in Section VI the conclusions are presented.

II. Modeling of Intruder's Signature

In this section, the time-varying heat flux signature generated by the intruder and the PIR sensor output signal are formulated.

A. PIR Sensor

A pyroelectric infrared sensor is a type of thermal sensor that reacts to the *change* in the sensor's temperature. Pyroelectric materials consist of crystals with ionic bonds that

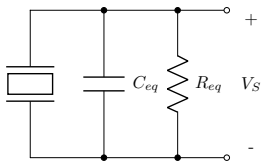

Fig. 1: PIR sensor electrical equivalent circuit.

are relatively separated, hence creating an electrical dipole moment. However, when exposed to a temperature change the structure of the crystals also changes thus modifying the polarization. The polarization in turn generates an electric displacement field that redistributes the charges on the sensor's surfaces creating a small current. This current is usually turned into a voltage through the use of a pre-amplifier circuit, included in modern PIR sensors. The change of the PIR sensor temperature results from incident heat flux emanating from an external (remote) source. A succinct discussion of the above is provided in [24] and extensive details can be found in [2].

The incident thermal flux is partially absorbed and converted into heat. However some of this heat is lost due to thermal convection in the sensor. This behavior is described by the following first order linear differential equation

$$\alpha\Delta\phi(t) = C_{Th}\frac{d}{dt}\Delta T_S\left(t\right) + G_{Th}\Delta T_S\left(t\right) \tag{1}$$

where $0 < \alpha < 1$ is the absorption factor, C_{Th} is the thermal heat capacity, G_{Th} is the thermal conductivity, $\Delta\phi(t)$ is the change in heat flux and $\Delta T_S\left(t\right)$ is the change in the sensor's temperature. As mentioned earlier, the temperature difference creates a displacement current due to the pyroelectricity property. Assuming zero initial voltage in the pyroelectric crystal, the pyroelectric current is given by

$$\begin{aligned} I_P\left(t\right) &= \frac{dQ}{dt} = A_S\frac{dD}{dt} \\ &= \pi_p A_S\frac{d\Delta T_S}{dt} \end{aligned} \tag{2}$$

where Q is the surface charge on the crystal, D is displacement current magnitude, A_S is the sensor's area and π_p is the pyroelectricity constant.

Now turning to the electrical properties of the PIR crystal, for a given pre-amplifier, its output voltage $(V_S(t))$ obeys the following:

$$C_{eq}\frac{d}{dt}V_S(t) + \frac{V_S(t)}{R_{eq}} = I_P(t) \tag{3}$$

where C_{eq} and R_{eq} are the equivalent capacitance and resistance of the PIR crystal and pre-amplifier, respectively, as shown in Fig. 1.

In summary, equations (1), (2) and (3) represent the transformation process from heat flux to voltage in the PIR sensor. In the frequency domain, these relationships are given by

$$\Delta T_S\left(\omega\right) = \frac{\alpha\Delta\Phi\left(\omega\right)}{j\omega C_{Th} + G_{Th}} \tag{4}$$

$$I_P(\omega) = j\omega\pi_p A_S\Delta T_S\left(\omega\right) \tag{5}$$

$$V_S(\omega) = \left(\frac{R_{eq}}{1 + j\omega R_{eq}C_{eq}}\right) I_P(\omega) \tag{6}$$

where $\Delta\Phi\left(\omega\right)$ is the change in the flux in the frequency domain. The overall conversion process is captured by the PIR sensor responsivity that is the system's transfer function

$$H(\omega) = \frac{V_S(\omega)}{\Delta\Phi(\omega)} \tag{7}$$

So, the transfer function takes the form

$$\begin{aligned} H(\omega) &= \frac{j\omega\alpha\pi_p A_S R_{eq}}{\left(1 + j\omega R_{eq}C_{eq}\right)\left(G_{Th} + j\omega C_{Th}\right)} \\ &= K\frac{j\omega\tau_{Th}}{\left(1 + j\omega\tau_E\right)\left(1 + j\omega\tau_{Th}\right)} \end{aligned} \tag{8}$$

where

$$K = \alpha\pi_p A_S\left(\frac{R_{eq}}{C_{Th}}\right) \tag{9}$$

$$\tau_E = R_{eq}C_{eq} \tag{10}$$

$$\tau_{Th} = C_{Th}/G_{Th} \tag{11}$$

are the PIR sensor gain, thermal time constant and electrical time constant respectively. Note that the sensor behaves as a bandpass filter with a lower cutoff frequency of $f_{Th} = 1/2\pi\tau_{Th}$ Hz and an upper cutoff frequency of $f_E = 1/2\pi\tau_E$ Hz.

B. Intruder Heat Flux

We are interested in measuring the heat flux generated by a non-manoeuvring intruder moving with constant speed and direction. The intruder is assumed to be in thermal equilibrium with its environment. The measured flux at the sensor mainly depends on the temperature, source geometry, and the spatial orientation of the intruder and the sensor with respect to (w.r.t.) each other. Assuming a Lambertian grey body emitting uniformly in space, the heat flux at the sensor is [2], [23]

$$\phi = \frac{1}{\pi}\varepsilon k_B\omega_{int,s}\left(T_{int}^4 - T_e^4\right)A_{int} \tag{12}$$

where $0 < \varepsilon < 1$ is the intruder's emissivity, $k_B \approx 5.67 \times 10^{-8}$Watt/(m^{2}Kelvin^4) is the Stefan-Boltzmann constant, T_{int} is the intruder's absolute temperature, T_e is the environment's temperature, A_{int} is the intruder's surface area, and $\omega_{int,s}$ is the projected solid angle of the intruder onto the sensor, describing the geometry of the source w.r.t. the sensor:

$$\omega_{int,s} = \frac{1}{A_s}\int_{A_{int}}\int_{A_s}\frac{\cos\beta_{int}\cos\beta_s}{R_{int,s}^2}dA_s dA_{int} \ . \tag{13}$$

Here A_s is the sensor's area, β_{int} and β_s are the angles of the infinitesimal elements dA_{int} and dA_s w.r.t. to the axis connecting them, and $R_{int,s}$ is the distance separating dA_{int} and dA_s. Consequently, the total heat flux is found by solving the double integration above and substituting into (12).

For an arbitrary geometry, the incident heat flux at the sensor can be approximated, for a distance (R) between the intruder and the sensor of more than 5 meters, as [23]

$$\phi \approx \varepsilon k_B\left(T_{int}^4 - T_e^4\right)\frac{A_{int}A_s}{4R^2} \tag{14}$$

which is simply an inverse square law relationship.

As the intruder passes in front of the PIR sensor, a Fresnel lens modulates the incident heat flux by partitioning the FOV into multiple segments[1] as shown in Fig. 4, where each segment concentrates the flux onto the PIR sensor. Consequently, the PIR sensor's signal depends on the intruder's trajectory through the FOVs and becomes time dependent (see (16)). Take for example an intruder crossing the central FOV segment with constant speed v making an angle ψ_0 with the main sensor axis at distance R_0 as shown in Fig. 3. The squared distance between the intruder and the sensor is given by the cosine rule [19] as

$$R^2(t) = v^2t^2 + \left(\frac{R_0 \sin\psi_0}{\sin(\psi_0+\xi)}\right)^2 + \frac{2vtR_0\sin\psi_0}{\tan(\psi_0+\xi)} \quad (15)$$

where ξ is the angle between the first FOV axis at which the intruder enters and the main sensor axis. So, for example ξ will be γ (which is the half FOV angle) for the single FOV case shown in Fig.3 and $3\gamma+\theta$ for the case shown in Fig.4 where θ is the half angle of the dead band (i.e., no flux signal in this angle region). Therefore, the incident heat flux has the form

$$\phi(t) = \frac{\phi_0}{R^2(t)}\left[\Pi\left(\frac{t-t_0}{d_0^+/v}\right) - \Pi\left(\frac{t-t_0-d_0^+/v}{d_0^-/v}\right)\right] \quad (16)$$

where

$$\phi_0 = \frac{\varepsilon k_B A_{int} A_s}{4}\left(T_{int}^4 - T_e^4\right) \quad (17)$$

and t_0 is the entry time. In addition

$$\Pi(t) = \begin{cases} 1,\ t\in[0,1] \\ 0,\ \text{otherwise} \end{cases} \quad (18)$$

with d_0^+ and d_0^- the distances the intruder travels in the positive and negative segments in the FOV as shown in Fig. 3.

In general, for $2F+1$ FOV segments indexed by $j = -F,\cdots,F$, we have the heat flux signature in the form

$$\phi(t) = \frac{\phi_0}{R^2(t)}\sum_{j=-F}^{F}\left[\Pi\left(\frac{t-t_j}{d_j^+/v}\right) - \Pi\left(\frac{t-t_j-d_j^+/v}{d_j^-/v}\right)\right] \quad (19)$$

where t_j is the jth segment entry time.

C. PIR Signal

As stated earlier, the PIR sensor converts the impinging heat flux into an electrical voltage. Therefore, the output voltage signal is a filtered version of the heat flux in (19), i.e.,

$$s(t) = h(t) * \phi(t) \quad (20)$$

where $h(t)$ is the sensor's time-domain responsivity (i.e., impulse response) and " $*$ " is the convolution operator. The PIR sensor elements are usually followed by a JFET voltage buffer, which superimposes the sensor signal onto a dc bias of the transistor. Also, the signal is corrupted by noise, which is dependent on the sensor and the environment background heat radiation. However, we assume that the voltage signal $(p(t))$ at the input to the analog to digital converter is appropriately conditioned to remove the dc bias, reduce the noise and amplify the signal by a proper gain (G) before being sampled at frequency $F_s = \frac{1}{T}$. Hence,

$$p[n] = Gs[n] + w[n] \quad (21)$$

for $0 \le n \le N-1$ where $s[n] = s(nT)$ with $w[n]$ assumed to be additive white Gaussian noise (AWGN) with zero mean and known variance (σ^2).

III. PIR Signal Preprocessing Chain

Obviously, the PIR signals in (20) and (21) do not lend themselves to analysis, due to the sensor filtering effect and noise. So, a block diagram illustrating the localization and tracking algorithm is shown in Fig. 2, part of which deals with the relevant aspects of deconvolution and denoising.

A. Signal Deconvolution

The PIR sensor impulse response $(h(t))$ can be obtained from the sensor's data sheet such as [25]. Given this information, a deconvolution filter can be used to reverse the effect of the PIR sensor to retrieve the original flux signal in (19). However, simply inverting the transfer function will not yield a causal filter[2]. To circumvent this problem, the inverted transfer function $H_{inv}(s)$ is composed of two steps. The first step $(H_{inv,1})$ is the reciprocal of $H(s)$ divided by s, which is given as follows:

$$H_{inv,1}(s) = \frac{(1+\tau_{Th}s)(1+\tau_E s)}{s^2} \quad . \quad (22)$$

Then, the second step is taking the derivative of the output of the transfer function $H_{inv,1}(s)$. This is accomplished by setting the second stage to $H_{inv,2} = s$. Thus, the full deconvoluation stage is given by

$$H_{inv}(s) = H_{inv,1}(s)H_{inv,2}(s)$$

which is actually the reciprocal of $H(s)$ leading to canceling the convolution step (i.e., deconvolving the PIR signal output). Then, $H_{inv}(s)$ is discretized via the bilinear transformation [26] to provide the digital deconvolution filter $h_{inv}[n]$. Eventually, the deconvolved signal is

$$\widehat{\phi}_d[n] = h_{inv}[n] * p[n] \quad (23)$$

where this signal still contains a noisy version of the flux signal.

B. Signal Denoising

In order to *clean* the flux signal and reduce the corrupting noise, we use a two-step denoising process. The first one utilizes the discrete wavelet transform based denoising (i.e., the wavelet coefficients are thresholded) where the Daubechies wavelet is used in conjunction with James-Stein block thresholding[3] [27], [28]. Note that the Daubechies wavelet is chosen

[1] In the context of intrusion detection, such an arrangement increases the probability of detection.

[2] For causality, $H(s)$ must be proper (i.e., the degree of the numerator must not exceed that of the denominator).

[3] This is readily available in the MATLAB Wavelet Toolbox.

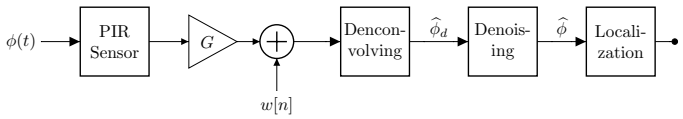

Fig. 2: Block diagram for the proposed localization and tracking algorithm.

since it can handle "jumps" in the received signal (when the intruder enters or leaves the FOV).

To discuss the second denoising step it is worth mentioning that the flux is a smooth piece-wise linear signal. Thus, we should look for a *smooth* signal that best fits the noisy one. This can be done via regression with a smoothing regularization. Fortunately, this amounts to solving the following convex optimization problem [29]:

$$\min_{\widehat{\boldsymbol{\phi}}} \|\widehat{\boldsymbol{\phi}}_{dd} - \widehat{\boldsymbol{\phi}}\|_2 + \lambda \|\mathbf{D}\widehat{\boldsymbol{\phi}}\|_1 \tag{24}$$

where $\widehat{\boldsymbol{\phi}}_{dd}$ is the output vector of the first denoising step and $\widehat{\boldsymbol{\phi}}$ is the final output vector of the smoothed flux signal. Also, λ is a regularization factor, $\|\cdot\|_2$ is the l_2 norm, $\|\cdot\|_1$ is the l_1 norm and $\mathbf{D}$ is the difference $((N-1)\times N)$ matrix used to enforce the smoothing condition and is defined as

$$\mathbf{D} = \begin{bmatrix} -1 & 1 & 0 & \cdots & 0 & 0 & 0 \\ 0 & -1 & 1 & \cdots & 0 & 0 & 0 \\ \vdots & \vdots & \vdots & & \vdots & \vdots & \vdots \\ 0 & 0 & 0 & \cdots & -1 & 1 & 0 \\ 0 & 0 & 0 & \cdots & 0 & -1 & 1 \end{bmatrix}. \tag{25}$$

Note that the l_1 norm is used above in the smoothing regularization term to preserve the piece-wise nature of the flux signal. In contrast to using the l_2-norm in the second term in (24) (also known as Tikhonov regularization), the use of the l_1-norm preserves the large variation inherent in the PIR signal. But Tikhonov regularization penalizes any large variation, so if used it will distort the output signal.

IV. Intruder Localization and Tracking Method

In this section we will illustrate the localization and tracking algorithm using the geometry of the PIR sensor's FOVs. In order to simplify the discussion we will first assume that ϕ_0 in (17) is known and derive the localization and tracking method. Then we will extend it to the general case where ϕ_0 is unknown.

A. Localization with pre-knowledge of ϕ_0

Consider the geometry in Fig. 3, which shows the intruder trajectory in a single FOV of the PIR sensor (for sake of illustration). Let the PIR sensor be located at the origin $(0,0)$. Having the (denoised) heat flux at hand and knowledge of ϕ_0 together with the fact that the signature flux in (19) reduces to ϕ_0/R_{-1}^2 where R_{-1} is the distance between the sensor and the entry point (x_{-1}, y_{-1}) then

$$y_{-1} = R_{-1}\cos\gamma \tag{26}$$

where γ is the half FOV angle as shown in Fig. 3. Consequently, it can be shown that

$$x_{-1} = -y_{-1}\tan\gamma \ . \tag{27}$$

Similarly, given the flux value at the exit point (x_1, y_1), one can deduce that

$$y_1 = R_1\cos\gamma \tag{28}$$

$$x_1 = y_1\tan\gamma \tag{29}$$

where R_1 is the distance between the exit point and the sensor.

The same procedure can be followed to find the transition point (x_0, y_0) which is the point between the positive and negative FOVs. Note that $x_0 = 0$ (from Fig 3). Also, one can easily deduce that $y_0 = R_0$ where R_0 is the distance between the transition point and the sensor.

Once the coordinates (x_{-1}, y_{-1}), $(0, y_0)$ and (x_1, y_1) are calculated, one can deduce the distances traveled by the intruder in the two halves of the FOV as shown in Fig. 3, i.e., d_j^+ and d_j^-. Thus, we can track the intruder trajectory.

The same process can be applied for each FOV to get the full track of the intruder. To generalize to the case of multiple FOVs the relation between the intruder track coordinates in all FOVs can be written in terms of R_0 (which is shown in Fig. 4) and the angle Ψ, which is the angle at which the intruder is passing with respect to the horizon (*x*-axis). According to the geometry in Fig. 4, the coordinates at which the intruder passes through the FOVs are given by

$$x_i = R_i\sin(u_i) \tag{30}$$

where $i = ..., -1, 0, 1, ...$, and

$$y_i = R_i\cos(u_i) \tag{31}$$

where

$$u_i = \text{sgn}(i)\left(|i| - \lfloor\frac{|i|+1}{3}\rfloor\right)\gamma + \text{sgn}(i)\lfloor\frac{|i|+1}{3}\rfloor\theta \tag{32}$$

and

$$R_i = \frac{R_0}{\cos(u_i) - \tan(\Psi)\sin(u_i)} \tag{33}$$

and where sgn is the sign function and $\lfloor . \rfloor$ is the floor operator.

B. Localization without pre-knowledge of ϕ_0

To localize the intruder without knowing the value of ϕ_0, we utilize the signals received by two sensors (as shown in Fig. 5). Without loss of generality we will assume that the locations of the first and second sensors are $(0,0)$ and $(B,0)$, respectively. The intruder passes through the FOVs of the first and second sensors at an angle Ψ as illustrated in Fig. 5. In this figure we show the principal FOV only in each sensor for the sake of clarity of explanation. However, the proposed method applies for the general case of multiple FOVs.

In order to find the coordinates of the intruder we need to estimate ϕ_0. Once, it is estimated, the method in the previous subsection can be readily applied. According to Fig. 5, the angle Ψ is constant throughout the path. Given the signal

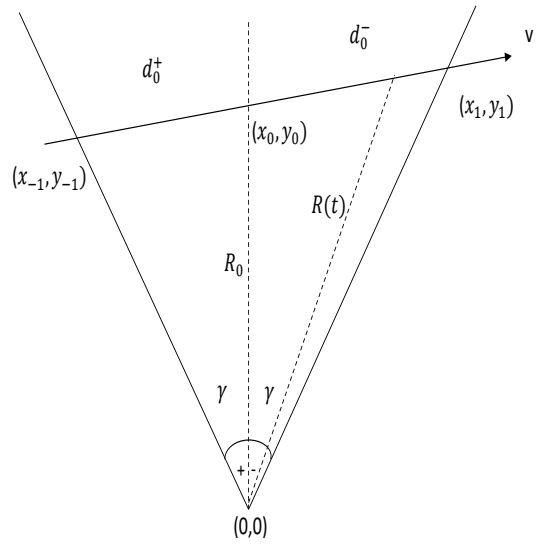

Fig. 3: Geometry for a single FOV.

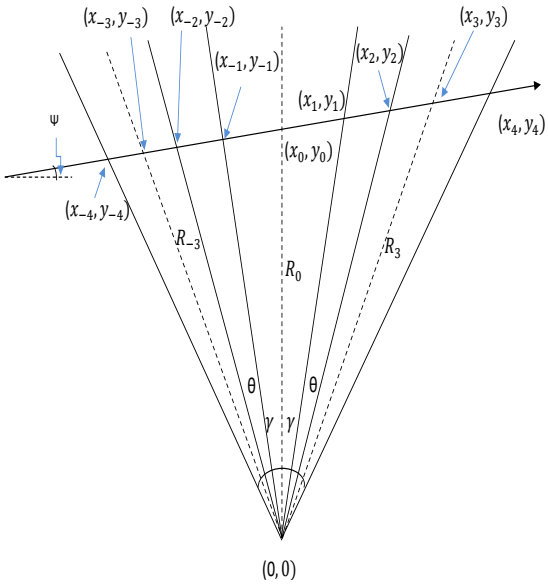

Fig. 4: Geometry for three FOVs.

strengths at the FOVs exit points extracted by the denoising process in Section III.B, one can state that

$$\tan\Psi = \frac{y_1 - y_{-1}}{x_1 - x_{-1}} = \frac{\frac{y_1}{\sqrt{\phi_0}} - \frac{y_{-1}}{\sqrt{\phi_0}}}{\frac{x_1}{\sqrt{\phi_0}} - \frac{x_{-1}}{\sqrt{\phi_0}}} \tag{34}$$

$$= \frac{c_{y,1} - c_{y,-1}}{c_{x,1} - c_{x,-1}} \tag{35}$$

where $c_{y,i} = \frac{y_i}{\sqrt{\phi_0}}$ and $c_{x,i} = \frac{x_i}{\sqrt{\phi_0}}$ are the square roots of the reciprocals of the extracted signal strength. Thus, the angle Ψ can be estimated since the right-hand-side of equation (35) is known.

Furthermore, at the first sensor we have

$$\tan\Psi = \frac{y_1}{x_1 + A} = \frac{c_{y,1}}{c_{x,1} + \tilde{A}} \tag{36}$$

where $\tilde{A} = \frac{A}{\sqrt{\phi_0}}$ and A is the distance between the first sensor and the intersection point between the x-axis and the extension of the intruder path (note here that without loss of generality the two sensors are located on the x-axis).

Now, since Ψ has been estimated, the unknown quantity $\tilde{A}$ can be found as well.

Similarly, given that B is the distance between the first and second sensors, it is easily shown that

$$\tan\Psi = \frac{\bar{y}_1}{\bar{x}_1 + A + B} = \frac{\bar{c}_{y,1}}{\bar{c}_{x,1} + \tilde{A} + \tilde{B}} \tag{37}$$

where $\bar{c}_{y,i} = \frac{\bar{y}_i}{\sqrt{\phi_0}}$, $\bar{c}_{x,i} = \frac{\bar{x}_i}{\sqrt{\phi_0}}$ and $\tilde{B} = \frac{B}{\sqrt{\phi_0}}$. So, rearranging (37) yields

$$\tilde{B} = \bar{c}_{y,1}\cot\Psi - \bar{c}_{x,1} - \tilde{A} \ . \tag{38}$$

Now given the recently estimated values, Ψ and $\tilde{A}$ and the already known B, it can be shown that

$$\phi_0 = \left(\frac{B}{\tilde{B}}\right)^2 \ . \tag{39}$$

Once ϕ_0 is estimated, then all the coordinates (x_i, y_i) and $(\bar{x}_i, \bar{y}_i)$ for $i = -1, 0, 1$ can be calculated. Thus, the intruder can be tracked without pre-knowledge of ϕ_0 as required.

Due to noise, the estimated coordinates (x_i, y_i) cease to be collinear and so do the variables $(c_{x,i}, c_{y,i})$. Thus, $\hat{\Psi}$ is estimated using the least squares method as follows:

$$\hat{\Psi} = \arctan\left(\frac{N_p \sum_i c_{x,i}c_{y,i} - \sum_i c_{x,i}\sum_i c_{y,i}}{N_p \sum_i c_{x,i}c_{x,i} - \sum_i c_{x,i}^2}\right) \tag{40}$$

where N_p is the total number of points considered which are indexed by i, i.e., for example $N_p = 9$ for the case shown in Fig. 4.

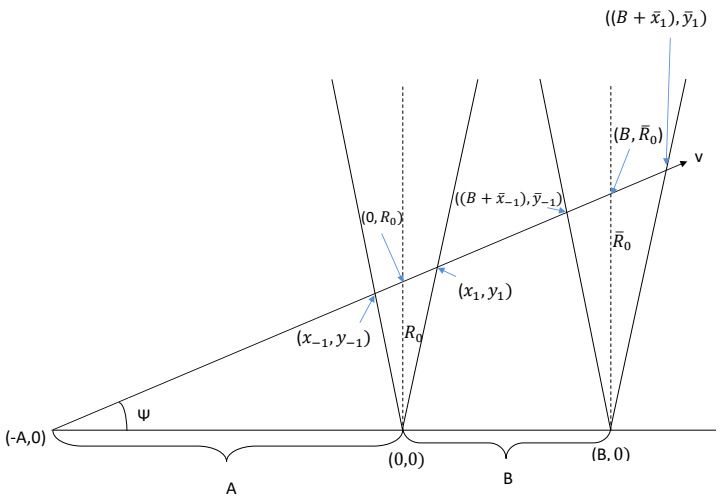

Fig. 5: Geometry for the proposed localization method.

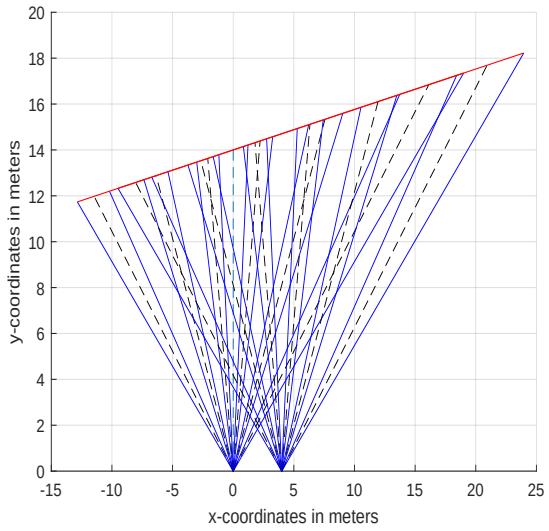

Fig. 6: FOVs with the intruder track.

Also, $\tilde{A}$ in (36) is estimated for each variable pair $(c_{x,i}, c_{y,i})$ together with using $\hat{\Psi}$ and is given the notation $\tilde{A}_i$. Then, we take the average value of $\tilde{A}_i$ for all i to find $\hat{A}$ which is the estimated value for $\tilde{A}$.

Accordingly, the estimated value of $\tilde{B}$ in (38) is given the notation $\hat{B}$ and calculated by using the average values of $\bar{c}_{x,i}$ and $\bar{c}_{y,i}$ instead of $\bar{c}_{x,1}$ and $\bar{c}_{y,1}$, respectively. Also, Ψ and $\tilde{A}$ are replaced with $\hat{\Psi}$ and $\hat{A}$, respectively. Thus,

$$\hat{\phi}_0 = \left(\frac{B}{\hat{B}}\right)^2 . \tag{41}$$

Now, this estimated variable $\hat{\phi}_0$ is used to find all the coordinates (x_i, y_i) and $(\bar{x}_i, \bar{y}_i)$ for $i = -1, 0, 1$ to locate and track the intruder.

V. Simulation Results

In this section, we present simulation results for tracking of a human intruder via the use of an array of two PIR sensors. The first sensor is located at the origin and the second sensor is located at (4m,0m). Each sensor has $F = 6$ FOVs and a half FOV angle of $\gamma = 7.5^o$, as shown in Fig. 6. The sensor area is $A_s = 20\mu\text{m}^2$ with emissivity of $\varepsilon = 1$ at environment temperature $T_e = 20^o$C. The PIR sensor has a gain of $K = 10^3$, with thermal and electrical time constants of $\tau_{Th} = 4.2$ sec and $\tau_E = 1$ sec, respectively. The sensor's thermal noise standard deviation is $\sigma = 0.5$mV (which results in normalized SNR of 23.9dB at $R_0 = 1$m). The intruder, on the other hand, has a temperature of $T_{int} = 37^o$C and a surface area of $A_{int} = 0.7\text{m}^2$. It moves with a constant speed of $v = 1$ km/hour in a straight line making angle with the x-axis of $\Psi = 10^0$.

In Fig. 7 we show the received heat flux signal of the intruder. The dashed lines represent the envelope of the thermal received flux. Due to the intruder's movement, the distance to the PIR sensor changes, which in turn changes the received heat flux amplitude (envelope) accordingly. The solid line on the other hand, represents the modulated received thermal flux due to having positive and negative elements in the PIR sensor. Fig. 8 illustrates the noisy PIR sensor output voltage signal resulting from the input heat flux shown in Fig. 7.

The corresponding deconvolved and denoised signal are shown in Fig. 9 where the first denoising step was performed using the James-Stein block algorithm with the first Daubechies wavelet type and 5 levels. As for the second denoising step, the regularization parameter in (24) is $\lambda = 0.15$. We instrumented the CVX MATLAB package [30] to solve the convex optimization problem in (24). Figs. 10, 11 and 12 illustrate the mean squared error (MSE) estimates of ϕ_0, R_0 and Ψ, respectively. The proposed algorithm performs extremely well in estimating ϕ_0 and Ψ in the range of 10^{-10} and 10^{-2}, respectively[4]. Notably, the localization error is in the sub-meter range, even at distances as far as 12m.

As expected, the MSE increases as the distance R_0 and noise standard deviation increase. In general, the results indicate that our proposed algorithm estimated the intruder trajectory parameters with a high accuracy.

VI. Conclusion

In this paper we propose a mathematical model describing the heat flux signature generated by a moving intruder and a corresponding PIR output signal. This model was used to develop a localization and tracking algorithm using two PIR sensors with the geometry of their FOVs and without any knowledge of the intruder parameters. The algorithm retrieves the original heat flux signature via equalizing the PIR sensor

[4]Please note that ϕ_0 is in the range of 10^{-4} Watt.m^2 and the estimation error is less than 10^{-5} Watt.m^2 causing the MSE in ϕ_0 to be in the range of 10^{-10}Watt^2.m^4.

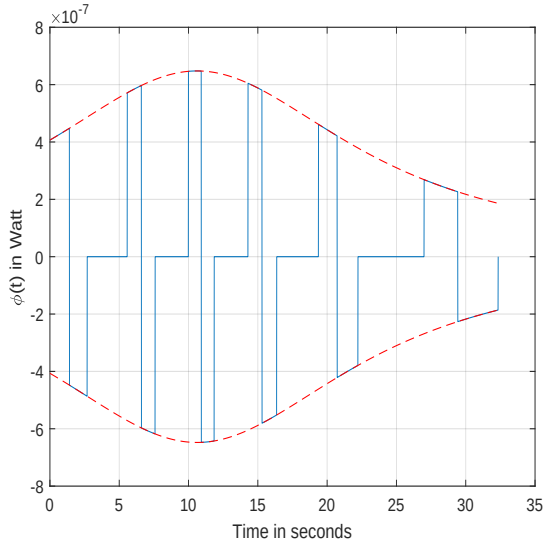

Fig. 7: Fresnel lens modulated signal (solid line) and the positive and negative input flux signal (dashed line) for $\Psi = 10^o$, $\sigma = 0.5$mV (normalized SNR=23.9dB) and $R_0 = 14$m.

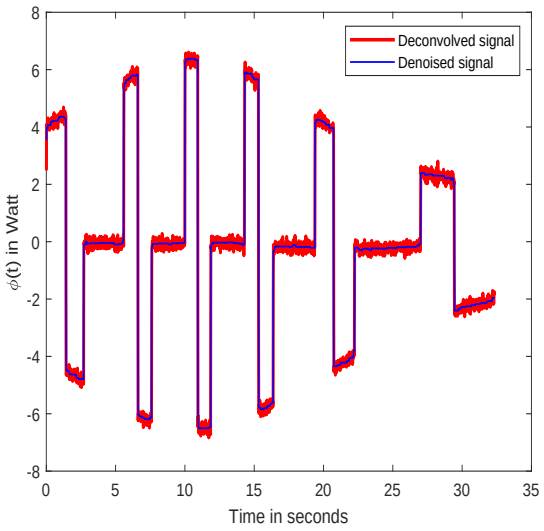

Fig. 9: Deconvolved and denoised signals $\Psi = 10^o$, $\sigma = 0.5$mV (normalized SNR=23.9dB) and $R_0 = 14$m.

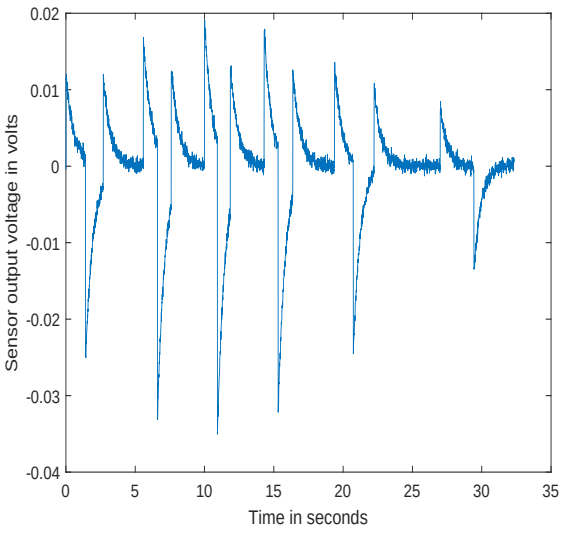

Fig. 8: PIR output signal $\Psi = 10^o$, $\sigma = 0.5$mV (normalized SNR=23.9dB) and $R_0 = 14$m.

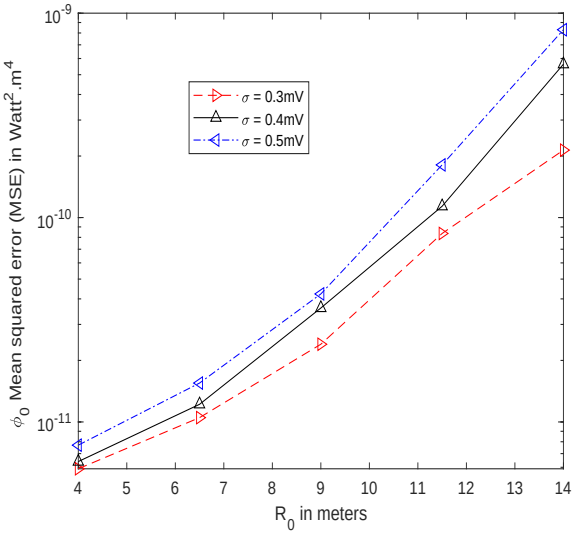

Fig. 10: MSE for ϕ_0 in Watt^2.m^4 vs. R_0 meters (where actual value for ϕ_0 is 1.23×10^{-4}Watt.m^2).

effect through deconvolution and denoising steps, which is then used for localization.

The proposed algorithm shows remarkable performance in estimating the intruder's parameters. The intruder heat flux was accurately estimated even at large separation distances. Moreover, the intruder path angle was estimated accurately as well. Finally, the intruder's location was estimated and tracked with sub-meter error for large separation distances.

REFERENCES

[1] A. Arora, P. Dutta, S. Bapat, V. Kulathumani, H. Zhang, V. Naik, V. Mittal, H. Cao, M. Demirbas, M. Gouda *et al.*, "A line in the sand: a wireless sensor network for target detection, classification, and tracking," *Computer Networks*, vol. 46, no. 5, pp. 605–634, 2004.

[2] H. Budzier, *Thermal infrared sensors theory, optimization, and practice*. Chichester, West Sussex, U.K. Hoboken, N.J: Wiley, 2011.

[3] D. Qu, B. Yang, and N. Gu, "Indoor multiple human targets localization and tracking using thermopile sensor," *Infrared Physics & Technology*, vol. 97, pp. 349 – 359, 2019. [Online]. Available: http://www.sciencedirect.com/science/article/pii/S1350449518308922

[4] A. Hossain and M. H. Rashid, "Pyroelectric detectors and their applications," *IEEE Transactions on Industry Applications*, vol. 27, no. 5, pp. 824–829, Sep. 1991.

[5] T. David Binnie, A. F. Armitage, and P. Wojtczuk, "A passive infrared gesture recognition system," in *2017 IEEE SENSORS*, Oct 2017, pp. 1–3.

[6] F. Erden and A. E. Cetin, "Hand gesture based remote control system using infrared sensors and a camera," *IEEE Transactions on Consumer*

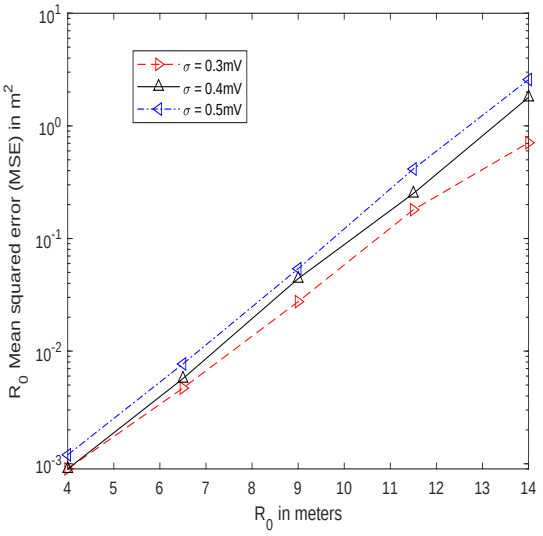

Fig. 11: MSE for R_0 in m^2 vs. R_0 meters.

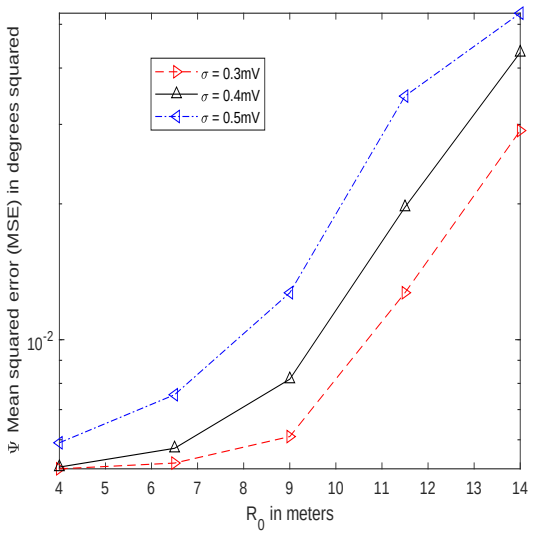

Fig. 12: MSE for Ψ in degrees squared vs. R_0 meters.

Electronics, vol. 60, no. 4, pp. 675–680, Nov 2014.

[7] F. Erden, S. Velipasalar, A. Z. Alkar, and A. E. Cetin, "Sensors in assisted living: A survey of signal and image processing methods," *IEEE Signal Processing Magazine*, vol. 33, no. 2, pp. 36–44, Mar. 2016.

[8] Y. P. Raykov, E. Ozer, G. Dasika, A. Boukouvalas, and M. A. Little, "Predicting room occupancy with a single passive infrared (pir) sensor through behavior extraction," in *Proceedings of the 2016 ACM International Joint Conference on Pervasive and Ubiquitous Computing*. ACM, 2016, pp. 1016–1027.

[9] Q. Hao, D. J. Brady, B. D. Guenther, J. B. Burchett, M. Shankar, and S. Feller, "Human tracking with wireless distributed pyroelectric sensors," *IEEE Sensors Journal*, vol. 6, no. 6, pp. 1683–1696, Dec. 2006.

[10] Q. Hao, F. Hu, and Y. Xiao, "Multiple human tracking and identification with wireless distributed pyroelectric sensor systems," *IEEE Systems Journal*, vol. 3, no. 4, pp. 428–439, Dec. 2009.

[11] J. Yun and M. Song, "Detecting direction of movement using pyroelectric infrared sensors," *IEEE Sensors Journal*, vol. 14, no. 5, pp. 1482–1489, May 2014.

[12] J. Xiong, F. Li, and J. Liu, "Fusion of different height pyroelectric infrared sensors for person identification," *IEEE Sensors Journal*, vol. 16, no. 2, pp. 436–446, Jan. 2016.

[13] S. Akbas, M. A. Efe, and S. Ozdemir, "Performance evaluation of pir sensor deployment in critical area surveillance networks," in *Distributed Computing in Sensor Systems (DCOSS), 2014 IEEE International Conference on*. IEEE, 2014, pp. 327–332.

[14] T. Choubisa, R. Upadrashta, S. Panchal, A. Praneeth, H. V. Ranjitha, K. Senthoor, A. Bhattacharya, S. V. R. Anand, M. Hegde, A. Kumar, P. V. Kumar, M. S. Iyer, A. Sampath, T. V. Prabhakar, J. Kuri, and A. N. Singh, "Challenges in developing and deploying a pir sensor-based intrusion classification system for an outdoor environment," in *2016 IEEE 41st Conference on Local Computer Networks Workshops (LCN Workshops)*, Nov 2016, pp. 148–155.

[15] X. Jin, S. Sarkar, A. Ray, S. Gupta, and T. Damarla, "Target detection and classification using seismic and pir sensors," *IEEE Sensors Journal*, vol. 12, no. 6, pp. 1709–1718, Jun. 2012.

[16] M. Mousa, X. Zhang, and C. Claudel, "Flash flood detection in urban cities using ultrasonic and infrared sensors," *IEEE Sensors Journal*, vol. 16, no. 19, pp. 7204–7216, Oct. 2016.

[17] E. Odat, J. S. Shamma, and C. Claudel, "Vehicle classification and speed estimation using combined passive infrared/ultrasonic sensors," *IEEE Transactions on Intelligent Transportation Systems*, vol. 19, no. 5, pp. 1593–1606, May 2018.

[18] L. Gu, D. Jia, P. Vicaire, T. Yan, L. Luo, A. Tirumala, Q. Cao, T. He, J. A. Stankovic, T. Abdelzaher *et al.*, "Lightweight detection and classification for wireless sensor networks in realistic environments," in *Proceedings of the 3rd international conference on Embedded networked sensor systems*. ACM, 2005, pp. 205–217.

[19] R. Abu Sajana, R. Subramanian, P. V. Kumar, S. Krishnan, B. Amrutur, J. Sebastian, M. Hegde, and S. Anand, "A low-complexity algorithm for intrusion detection in a pir-based wireless sensor network," in *Intelligent Sensors, Sensor Networks and Information Processing (ISSNIP), 2009 5th International Conference on*. IEEE, 2009, pp. 337–342.

[20] Q. Sun, F. Hu, and Q. Hao, "Mobile target scenario recognition via low-cost pyroelectric sensing system: Toward a context-enhanced accurate identification," *IEEE Transactions on Systems, Man, and Cybernetics: Systems*, vol. 44, no. 3, pp. 375–384, March 2014.

[21] P. Zappi, E. Farella, and L. Benini, "Tracking motion direction and distance with pyroelectric ir sensors," *Sensors Journal, IEEE*, vol. 10, no. 9, pp. 1486–1494, 2010.

[22] J. Yun and M.-H. Song, "Detecting direction of movement using pyroelectric infrared sensors," *Sensors Journal, IEEE*, vol. 14, no. 5, pp. 1482–1489, 2014.

[23] S. Aldalahmeh, A. Hamdan, M. Ghogho, and D. McLernon, "Enhanced-range intrusion detection using pyroelectric infrared sensors," in *Proc. Sensor Signal Processing for Defence (SSPD)*, Sep. 2016, pp. 1–5.

[24] A. Odon, "Modelling and simulation of the pyroelectric detector using matlab/simulink," *Measurement Science Review*, vol. 10, no. 6, pp. 195–199, 2010.

[25] MuRata, "Pyro electric infrared sensor fresnel lens," 2017.

[26] J. G. Proakis, *Digital signal processing: principles algorithms and applications*. Pearson Education India, 2001.

[27] T. T. Cai, "Adaptive wavelet estimation: a block thresholding and oracle inequality approach." *Annals of Statistics*, vol. 27, no. 3, p. 898–924, 1999.

[28] ——, "On block thresholding in wavelet regression: Adaptivity, block size, and threshold level." *Statistica Sinica*, vol. 12, no. 4, p. 1241–1273, 2002.

[29] S. Boyd and L. Vandenberghe, *Convex optimization*. Cambridge university press, 2004.

[30] M. Grant and S. Boyd, "CVX: Matlab software for disciplined convex programming, version 2.1," http://cvxr.com/cvx, Mar. 2014.